Desalination and Water Treatment
www.deswater.com
doi: 10.5004/dwt.2020.25316

183 (2020) 389–403
April

Nano-sized $Ga_{2-x}Cu_xZr_{2-x}W_xO_7$ for Malachite green decolorization under visible light

Rabab A. Nasr[a], H.A. Abbas[b,*], Aya Khalaf[c], Ayat Bozeya[c], Tarek S. Jamil[a]

[a]*Water Pollution Control Department, National Research Center, El Behouth Street, P.O. Box: 12622, Dokki, Cairo, Egypt, emails: rababelsheikh@yahoo.com (R.A. Nasr), omaytarek73@yahoo.com (T.S. Jamil)*
[b]*Inorganic Chemistry Department, National Research Centre, El-Behouth Street P.O. Box: 12622, Dokki, Cairo, Egypt, email: hu_abbas2005@yahoo.com (H.A. Abbas)*
[c]*Chemistry Department School of Science, The University of Jordan, Hamdi Mango Centre for Scientific Research, 11942, Amman, Jordan, emails: aya.khalaf89@yahoo.com (A. Khalaf), bozeyaayat@yahoo.com (A. Bozeya)*

Received 15 May 2019; Accepted 6 December 2019

ABSTRACT

Novel nano-sized $Ga_{2-x}Cu_xZr_{2-x}W_xO_7$ system was prepared using the Pechini method, where x = 0, 0.05, 0.1 and 0.015. A single cubic fluorite phase was detected for all the prepared samples. The lattice parameter and unit cell volume of the undoped $Ga_2Zr_2O_7$ is higher than that of Cu, W co-doped $Ga_2Zr_2O_7$ samples. The band gap was decreased from 4.95 eV for the undoped $Ga_2Zr_2O_7$ to 2.89 eV for $Ga_{1.85}Cu_{0.15}Zr_{1.85}W_{0.15}O_7$ sample (15 mole % Cu and 15 mole % W doped $Ga_2Zr_2O_7$), shifting the absorption edge to the visible light area. The photocatalytic degradation efficiency of $Ga_{2-x}Cu_xZr_{2-x}W_xO_7$ system for malachite green dye as a water contaminant model was presented. The photocatalytic activity of $Ga_{1.85}Cu_{0.15}Zr_{1.85}W_{0.15}O_7$ recorded 93.84% degradation of malachite green dye, which is higher than that of the undoped $Ga_2Zr_2O_7$ (16.66%). The photocatalytic degradation reaction for the malachite green dyes was inconsistent with the Pseudo-first-order kinetics model. The reusability of the prepared system as a catalyst was proven. The intermediates and the reaction pathways were detected by GC-MS.

Keywords: $Ga_2Zr_{2-x}W_xO_7$; Fluorite phase; Wastewater treatment; Nanomaterials; Malachite green dye

1. Introduction

Prevention or minimization of ecological pollution has been the focus of extensive research in recent decades. Dumping of dyes into water resources, even at trace concentrations, resulted in harmful effects, including high chemical oxygen demand (COD) and biological oxygen demand (BOD) organic loads, unfavorable odors, colored wastewater, all of which negatively influence the biodiversity in the ecosystem [1,2].

Malachite green (MG) is a cancer-causing organic dye frequently used as a colorant food additive, as well as colorant for paper and textile [3–6] Fig. 1. It is also utilized as a disinfectant against protozoa and parasites in the horticultural field [7]. The genotoxic and carcinogenic effects of MG have been confirmed for human reproductive and immune organs [8,9].

Imitative chemical and physical processing techniques utilized for decolorization of textile factory effluents produced non-biodegradable materials that could be more biologically harmful than the parent dyes and may acquire extra treatment [10–14].

Many techniques have been introduced for MG decolorization, including biosorption [15–17], ultrasonic irradiation [18], and sunlight irradiation [8,19]. Recently, advanced oxidation processes emerged as a promising technique for

* Corresponding author.

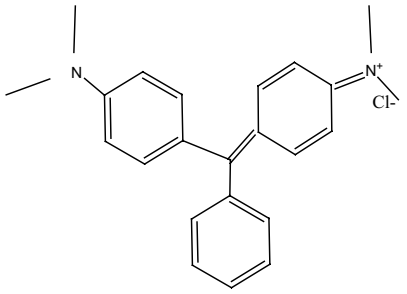

Fig. 1. Chemical structure of Malachite green.

the release of MG from wastewaters achieving total mineralization by hydroxyl radical generation [20].

During the heterogeneous photocatalytic process, semiconductor particles receive light photons of higher energy than their band gap. As a result, the electrons in semiconductor materials are excited from the valence band to conduction band creating charge carriers (electrons/hole), which leads to the creation of hydroxyl radicals which play an essential role in the mineralization of MG through oxidation [21,22].

Different photocatalytic materials were eventually introduced as photocatalysts for example, TiO_2, ZnS, ZnO, WO_3, V_2O_5, CdS [23], $KBiO_3$, $LiBiO_3$ [24], Graphene/ZnO Nanocomposite [25], Fe(III)-grafted *K*-doped g-C_3N_4/rGO composite [26], WO_3/g-C_3N_4 and CeO_2/g-C_3N_4 [27]. $A_2B_2O_7$ oxides are stabilized, whether in a pyrochlore-type or a defect fluorite-type structure depending on the ionic radius ration of the A and B cations (r_A/r_B ratio) [28]. The electrical properties of the pyrochlores fluctuated between extravagant insulation to metallic conduction. Pyrochlores metal oxides have been widely used as thermal barrier covering [29], host matrices for photoluminescence, and host material for fixation of nuclear waste outputs [30]. Luminescence properties of $Ln_2Ce_2O_7$ fluorite-type have been examined before [28]. Less consideration is being given to fluorite-type Zr-based oxides with $Ga_{2-x}Cu_xZr_{2-x}W_xO_7$ composition for different applications. In addition, the photocatalytic activity of fluorite-type structure $Ga_2Zr_{2-x}W_xO_7$ in the declination of MG color isn't accounted for yet.

The aim of the present work is to achieve MG decolorization using new photocatalysts, such as fluorite-type Zr based oxides with $Ga_{2-x}Cu_xZr_{2-x}W_xO_7$ composition nanoparticles prepared by the Pechini technique. The W and Cu co-doping impact on the structural properties of $Ga_2Zr_2O_7$ and the decolorization of MG dye in visible light are studied. The prepared materials were completely characterized and the impacts of the working parameters were optimized (contact time, pH, catalyst dosage, initial dye concentrations).

2. Experimental

2.1. Preparation and characterization of the prepared materials

$Ga_{2-x}Cu_xZr_{2-x}W_xO_7$ system was prepared using the citrate technique (Pechini method), which is a wet-chemical method based on polymeric precursor [31] that was used to prepare several metal oxides [32–36] where x = 0, 0.05, 0.15. In this method, α-hydroxy acid (citric acid) is used to chelate the cations forming a polybasic acid. Polyhydroxy alcohol (ethylene glycol) reacts with these chelates forming ester and water. Heating of the mixture leads to polyesterification and after the evolution of nitrous oxide and water, a gel is obtained. The thermal decomposition of this gel results in a chemically homogeneous powder containing the desired stoichiometry [32,33].

Zirconium (IV) oxynitrate hydrate (99%, Sigma-Aldrich, Canada), Tungsten (VI) chloride (99.9%, Sigma-Aldrich, Canada), Copper (II) nitrate trihydrate (98%, Scharlau Chemie S.A, Spain), Gallium (III) nitrate (99.9%, Silverton San Diego), Ethylene Glycol (99.8, ROAD, Sandy Croft, Deeside, CLWYD), Citric Acid Anhydrous Extra pure (99.5%, Loba Chemie, India), Ammonia (25% as NH_3, Panreac Quimica, Spain (PRS)) are used as starting materials. All chemicals were reagent grade and used as received without any modification.

$Ga_{2-x}Cu_xZr_{2-x}W_xO_7$ system was prepared using the Pechini method as follows: tungsten chloride was dissolved in ethanol. Aqueous zirconium oxynitrate, gallium nitrate, copper nitrate and tungsten chloride solutions were mixed, considering the desired stoichiometry of the metal oxides in the final ceramic powder solution. The citric acid (CA) was then added to the solution (A) to chelate metal cations at the CA:Me molar ratio of 4:1. Me denotes Ga^{3+}, W^{6+}, Cu^{2+} and Zr^{4+} in the final ceramic powder. After the dissolving of CA, the pH of the solution was adjusted to be 3 where a clear solution was obtained. Ethylene glycol (EG) was added into the solution at a CA: EG molar ratio of 1:1.5. The solution was then heated at 140°C and kept under stirring to promote the esterification and polymerization reactions. After the elimination of nitrous oxides and water, a gel was obtained. The gel was charred gradually up to 300°C then heated in the muffle furnace at 300°C for 2 h. The charred gel thus produced was grounded and calcined for 2 h at 500°C then ground and calcined for 2 h at 600°C. $Ga_2Zr_2O_7$ was prepared using the same sequence. The preparation flowchart for $Ga_{2-x}Cu_xZr_{2-x}W_xO_7$ powder is presented in the supplementary information Fig. S1.

2.2. Experimental set up of Photocatalytic degradation of dye

MG was obtained from Sigma-Aldrich Chemical Company, Canada. All solutions were prepared in doubly distilled water. Photocatalytic experiments were carried out with MG dye solution using all prepared catalysts under exposure to visible irradiation in the Pyrex glass beaker of 250 mL volume and the suspension was magnetically stirred. Irradiation was carried out using a commercial visible metal halide lamp (HQI-T250/Daylight, OSRAM GmbH, Germany) with a luminous efficacy of 82 lm/W and luminous flux of irradiation 20,000 lm (244 W) was used. During the photocatalytic experiment, after stirring for 10 min slurry composed of dye solution and catalyst was placed in the dark for 1/2 h in order to establish equilibrium between adsorption and desorption phenomenon of dye molecule on photocatalyst surface. As well, the effect of photolysis (effect of visible light irradiation on MG without catalyst) was carried out for 2 h in order to study the stability of MG. Then slurry containing aqueous dye solution and photocatalyst was stirred magnetically to ensure complete suspension of catalyst particle while exposing to visible light. At specific time intervals, an aliquot (5 mL) was withdrawn and centrifuged for

2 min at 3,500 rpm to remove photocatalyst particles from aliquot to assess the extent of decolorization photometrically. Changes in absorption spectra were recorded at 617 nm on double-beam UV-Vis. Spectrophotometer (Cary-100) a pH of the solution was measured using a digital pH meter. The desired pH of the solution was adjusted by the addition of previously standardized 0.050 M H_2SO_4 and 1.0 M NaOH solutions. Performance efficiency was calculated as:

$$\%\text{Efficiency} = \frac{C_0 - C}{C_0} \times 100 \quad (1)$$

where C and C_0 are initial and final dye concentration for reaction time t.

2.3. GC-MS analysis of MG by-products

The by-products formed during degradation of MG using ZGW2C2 sample were determined by Mass spectroscopy through full scan mode. The GC-MS analysis was performed using a GC-MS Varian 4,500, fused silica capillary column (30 m 0.25 mm, 0.25 μm film thickness equipped with an electron ionization system with ionization energy of 70 eV. Helium gas was used as carrier gas at a constant flow rate of 1 mL/min. The injector and MS transfer line temperature was set at 280°C. The oven temperature was programmed at an initial temperature of 40°C (hold 3 min) at 280°C as the final temperature at an increasing rate of 5°C/min (hold 5 min).

2.4. Phenol measurement

Phenol was determined after degradation of MG by Chromatography DIONX- ICS- 5,000+ DC according to APHA, 2017 [37].

3. Characterizations of prepared materials

X-ray diffraction (XRD) is used to identify the crystal structure, to determine the lattice parameters and the particle size of the prepared samples. The XRD measurements were carried out using 7,000 Shimadzu (Japan) 2 kW model X-ray spectrophotometer with a nickel filtered Cu radiation (CuKα) with λ = 1.54056 Å. The scanning 2θ range was 5–80 with a step size of 0.2. The lattice parameters were determined using a program called UnitCellWin [38]. The microstructures were studied by transmission electron microscopy (TEM, JEOL JEM2100). Diffuse reflectance measurements were performed to study the optical properties of the prepared samples using Shimadzu UV-3,600 (Japan). The specific surface area of the prepared samples was determined by NOVA Surface Area Analyzer from Thermo Pascal 140 mercury porosimetry under a pressure range of 0.1–200 MPa. Mercury surface tension of 480 Dyne/cm and contact angle of 141.3° were used. The binding energy of the elements was measured at room temperature by X-ray photoelectron spectroscopy (Thermo scientific *k*-alpha Al DHA). Energy dispersive X-ray spectroscopy (EDX) spectra, as well as the elemental mapping for the prepared samples, were obtained with a Quanta EFG250 scanning electron microscope equipped with a Link analytical system.

4. Results and discussion

4.1. Characterization of the prepared materials

4.1.1. X-ray diffraction

Fig. 2 shows the XRD pattern of ZG, ZGW1C1, and ZGW2C2, denoting $Ga_2Zr_2O_7$, $Ga_{1.95}Cu_{0.05}Zr_{1.95}W_{0.05}O_7$ and $Ga_{1.85}Cu_{0.15}Zr_{1.85}W_{0.15}O_7$ respectively. Cubic fluorite phase was detected for ZG sample (PDF 78-1299 for $Er_{0.5}Zr_{0.5}O_{1.75}$, which is the best-matched card that could be used, since there was no card for the novel $Ga_2Zr_2O_7$ material). The peaks of ZG sample are shifted to lower 2θ value as compared to $Er_{0.5}Zr_{0.5}O_{1.75}$ peaks. This might be due to the difference in the ionic radii between Er^{3+} (ionic radius = 89 pm [39]) and Ga^{3+} (ionic radius = 62 pm [39]) ions.

Fig. 2 shows that all prepared W, Cu co-doped $Ga_2Zr_2O_7$ samples (ZGW1C1 and ZGW2C2) were crystallized in the cubic fluorite phase (PDF 78-1,299). The cubic lattice parameter and unit cell volume for all the samples are calculated and presented in Table 1.

4.1.2. DRS Diffuse reflectance spectroscopy

Diffuse reflectance spectroscopy was used for studying the optical properties of the samples. Fig. 3 clarified that the absorption edge of the ZG sample is about 247 nm and co-doping by W and Cu shifted the absorption to the visible light range.

The band gap of the samples was obtained according to Kubelka-Munk [40] by plotting $F(R_\infty)E)^{1/2}$ against photo energy then linear fit was performed (Figs. 4 and S2 in the supplementary information). The obtained band gap is presented in Table 2. The band gap of the ZG sample

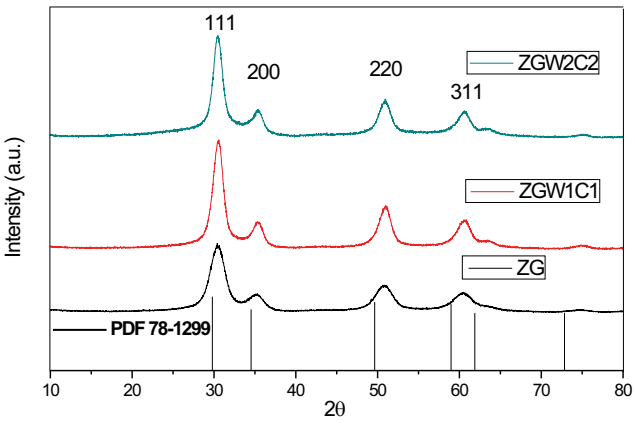

Fig. 2. Powder x-ray diffraction pattern of $Ga_{2-x}Cu_xZr_{2-x}W_xO_7$ system calcined at 600°C/2h (x = 0, 0.05 and 0.15).

Table 1
Microstructural parameters of $Ga_{2-x}Cu_xZr_{2-x}W_xO_7$ system

Sample	a (Å)	V (Å^3)
ZG	5.09539	132.2915
ZGW1C1	5.01212	125.9113
ZGW2C2	5.08101	131.1748

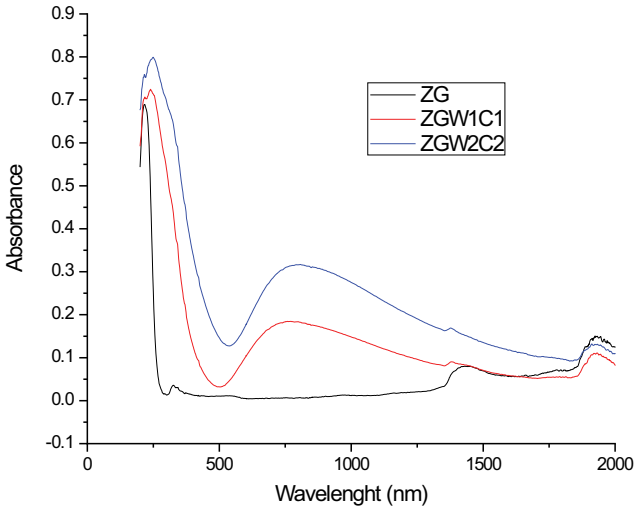

Fig. 3. Diffuse reflectance spectra of ZG, ZGW1C1 and ZGW2C2 samples.

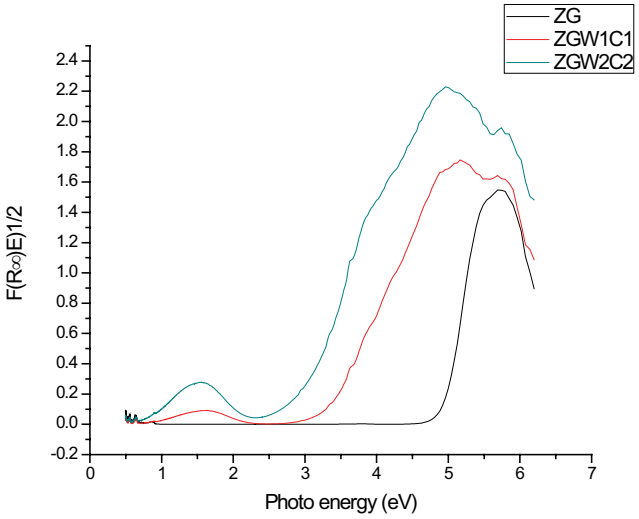

Fig. 4. Plots of $F(R_\infty)E^{1/2}$ vs. photo energy for the estimation of the band gap energy for ZG, ZGW1C1 and ZGW2C2 samples.

Table 2
Estimated band gap values for $Ga_{2-x}Cu_xZr_{2-x}W_xO_7$ system and the TEM particle size range

Sample	Band gap	Particle size range (nm)
ZG	4.95	4–7
ZGW1C1	3.41	5–8
ZGW2C2	2.89	4–6

was 4.95 eV. As the concentration of W and Cu increased, the band gap decreased. ZGW2C2 sample had the lowest band gap value (2.89 eV).

The band gap of Cu doped β-Ga_2O_3 (4.73 eV) was lower than that of the undoped β-Ga_2O_3 (4.83 eV). This decrease in the band gap (0.1 eV) could be attributed to the formation of an impurity energy level of Cu in the β-Ga_2O_3 [41].

ZrO_2 has a wide band gap (5 eV) which renders its absorption of visible light and, consequently, is not used as a photocatalyst in the visible light range [42,43]. The band gap of undoped $Ga_2Zr_2O_7$ is close to that of ZrO_2. In the present work, the fluorite structured W, Cu co-doped $Ga_2Zr_2O_7$ had smaller band gap than that of ZrO_2 and close to that of some pyrochlore structured oxides, such as $Sm_2Zr_2O_7$ (2.86 eV) and $Nd_2Zr_2O_7$ (2.67 eV) [44].

For $Sm_2Zr_2O_7$ and $Nd_2Zr_2O_7$, the conduction band composed of Zr 4d orbitals whereas the valence band consists of Sm or Nd 4f orbitals. The Sm or Nd 4f orbitals lie on the top of the O 2p bands thus raising the valence band level [44]. In the $Ga_{2-x}Cu_xZr_{2-x}W_xO_7$ system, new energy levels might be introduced from Cu on the top of O 2p bands and from W on the bottom of the conduction band resulting in decreasing the band gap. This is in agreement with that for $SrT_{i0.7}Fe_{0.3}O_3$ (30 mole % Fe doped $SrTiO_3$) [45], Ga doped and Sc doped $SrT_{i0.7}Fe_{0.3}O_3$ [46,47] and for Zr doped indium tin oxide (ITO) [48]. Fig. 5 shows the schematic diagram for band gap and the proposed new energy levels introduced by doping.

4.1.3. Transmission electron microscopy

Fig. S3 the supplementary information shows the TEM micrographs of all the prepared samples. Small quasi-spherical particles, which agglomerate into denser aggregates were observed. The particle size range determined by TEM for all samples is presented in Table 2. All the samples are in the small nano-sized range which is comparable to the XRD part. Fig. 6 shows the EDX and the elemental mapping of the ZGW2C2 sample. The EDX and the elemental mapping of ZG, ZGW1C1 samples are presented in the supplementary information (S4–S5). The well-defined peaks of Ga, Zr, W, Cu and O are evident in the presence of Ga, Zr, Cu, W and O in the prepared samples (Figs. 6 and S4). The homogeneous distribution of the elements is confirmed by the elemental mapping (Figs. 6 and S4 and S5).

Fig. 7 shows a typical X-ray photoelectron survey spectrum of ZG, ZGW1C1 and ZGW2C2 nanoparticle samples.

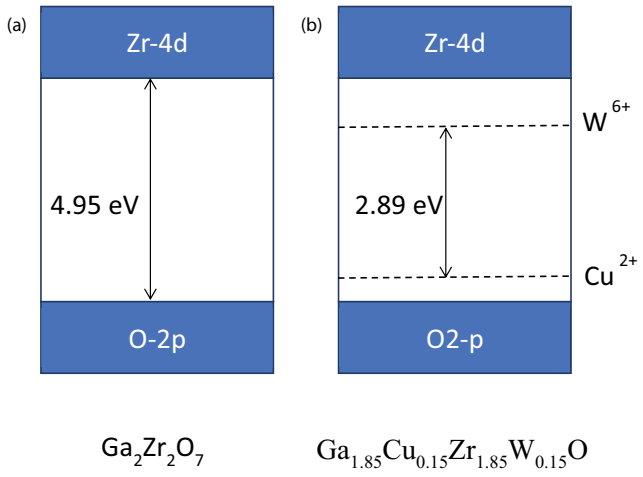

Fig. 5. Schematic diagram for band gap and the proposed new energy levels introduced by doping for (a) $Ga_2Zr_2O_7$ and (b) $Ga_{1.85}Cu_{0.15}Zr_{1.85}W_{0.15}O_7$ samples. The arrow represents the band gap.

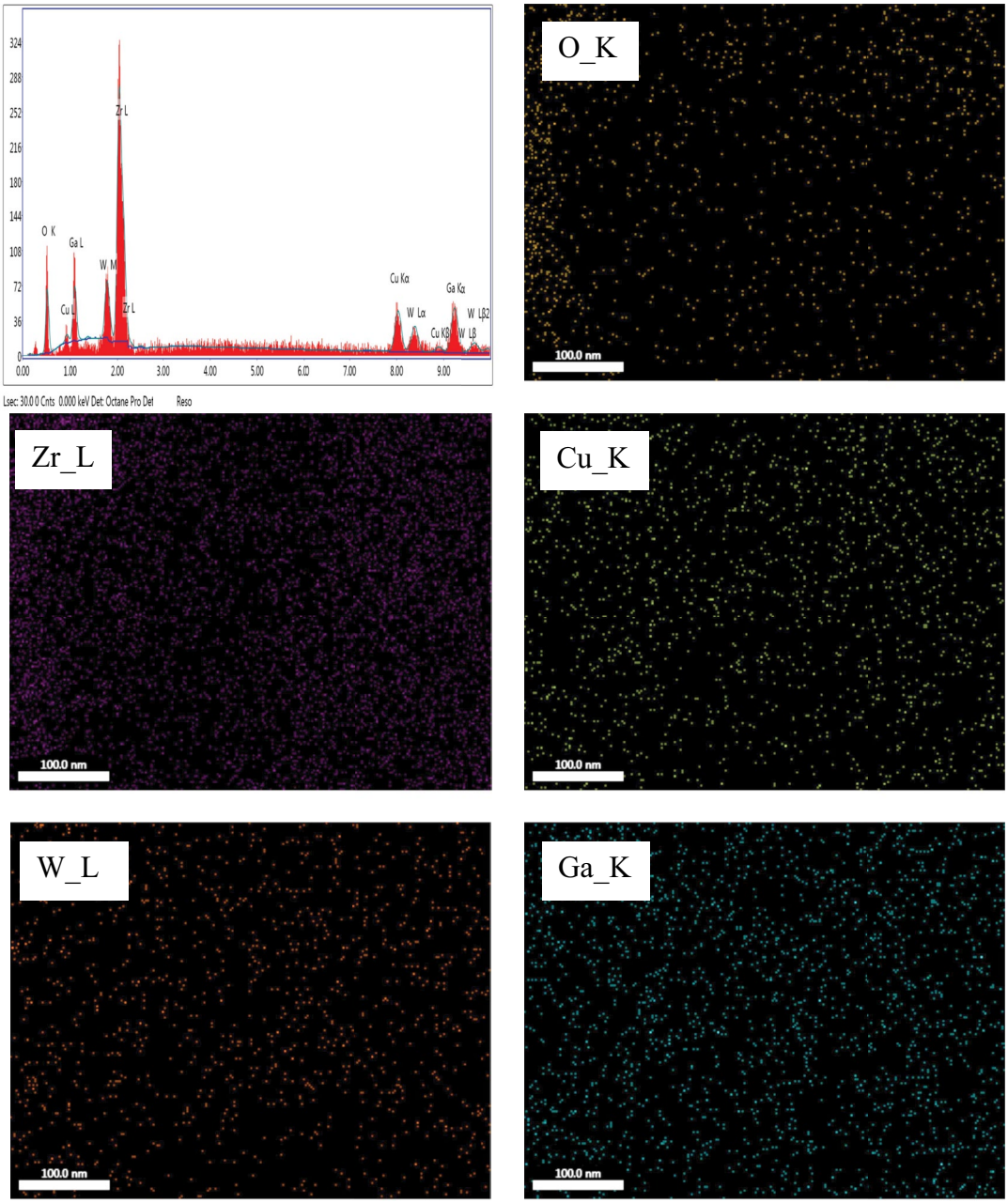

Fig. 6. The EDXs and elemental mapping of ZGW2C2 sample.

Cu2p and W4f core levels are not detected in the parent ZG sample. The high-resolution scans of W4f and Cu2p core levels of ZGW1C1 and ZGW2C2 samples are presented in Fig. 8a and b. Fig. 8a shows two peaks of $Cu2P_{3/2}$ and $Cu2P_{1/2}$ in addition, to a shake satellite at about 942 eV. Interestingly, the peak positions of $Cu2P_{3/2}$ and $Cu2P_{1/2}$ in addition to the presence of shake satellite characteristics of Cu^{2+} in the Cu2P spectra [49] is an indication that Cu exists as Cu^{+2}. Fig. 8b shows two peaks of $W4f_{5/2}$ (37.39 eV) and $W4f_{7/2}$ (35.2 eV) which corresponds to tungsten in the 6+ oxidation state [50]. The peak at 31.0 eV is characteristic of metallic tungsten [51] indicating that during the calcination of the precursors, some reduction of W took place. The elemental composition for ZG, ZGW1C1, and ZGW2C2 samples obtained from XPS analysis are presented in the supplementary information (Table S1).

From the XRD part, the cubic lattice parameter and unit cell volume for ZGW1C1 and ZGW2C2 samples were lower than that of the parent ZG sample. This might be attributed to the reduction of tungsten to metallic tungsten detected in the XPS analysis, resulting in the substitution of the larger Zr^{4+} ion (ionic radius = 72 pm) by the smaller W^{6+} ion (ionic radius = 60 pm [39]) and the substitution of Ga^{3+} ion (ionic radius = 62 pm [39]) by Cu^{2+} ion (ionic radius = 73 pm [39]), decreasing the cubic lattice parameter and unit cell volume.

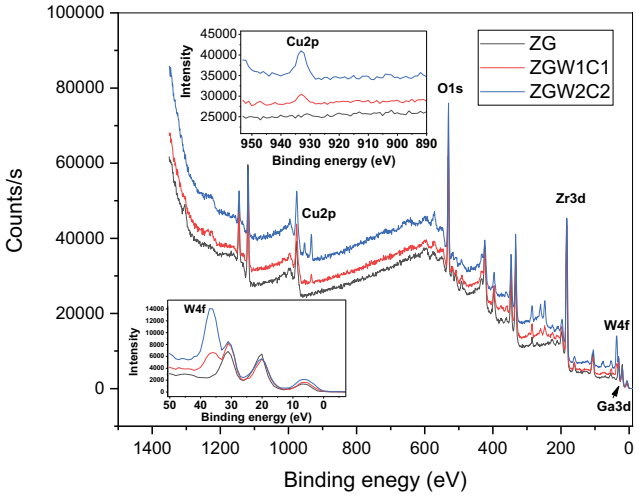

Fig. 7. X-ray photoelectron survey spectrum of ZG, ZGW1C1 and ZGW2C2 nanoparticle samples. In the inset, the Cu2p and W4f core levels spectrum are shown.

4.1.5. BET surface area

To manifest the surface area of the prepared oxides, the BJH Nitrogen adsorption tests were utilized in Fig. 9. A type-IV isotherm, with an H_3 type hysteresis loop, demonstrates the typical mesopores materials, that is related to aggregates presented in the mesopores [40,52]. Specific surface areas are 91.26, 62.7 and 68.1 m^2/g for ZG, ZGW1C1 and ZGW2C2 respectively.

4.2. Effect of different variables on photocatalytic degradation of dye

4.2.1. Degradation time effect

MG was stable under visible light without catalyst due to the non-significant change in dye concentration after 5 h. Since; mg/L MG dye was removed by <1% after 5 h).

The time impact of MG photodegradation was examined by the visible/ZG, ZGW1C1, and ZGW2C2 systems. Fig. 10 illustrates the degradation of MG between 0–480 min.

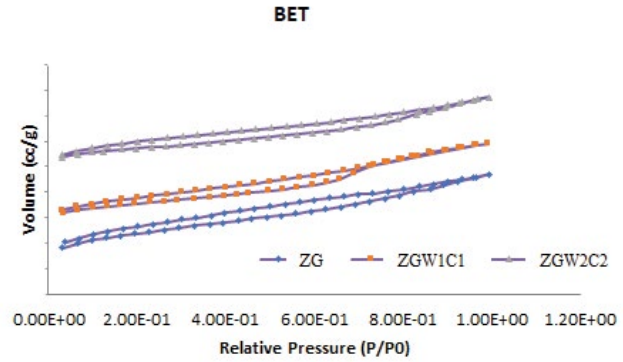

Fig. 9. N_2 adsorption and desorption isotherms for ZG, ZGW1C1, and ZGW2C2.

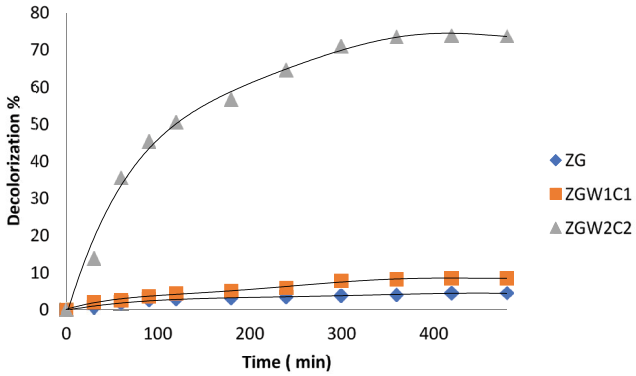

Fig. 10. The effect of reaction time on MG degradation at pH 5, 40 mg/L MG concentration and 0.75 g/L catalyst dose under visible light irradiation.

The photocatalytic MG degradation is improved with the increment of W and Cu concentration from 5 to 15 mol.% which leads to the creation of an excess amount of $O_2^{-\bullet}$ and $HO^{\cdot}$ radicals which is accountable to MG degradation.

W and Cu co-doping increased the electrons and holes de-trapping, which had positive influences on the photocatalytic performance of the $Ga_2Zr_2O_7$. The degradation rate

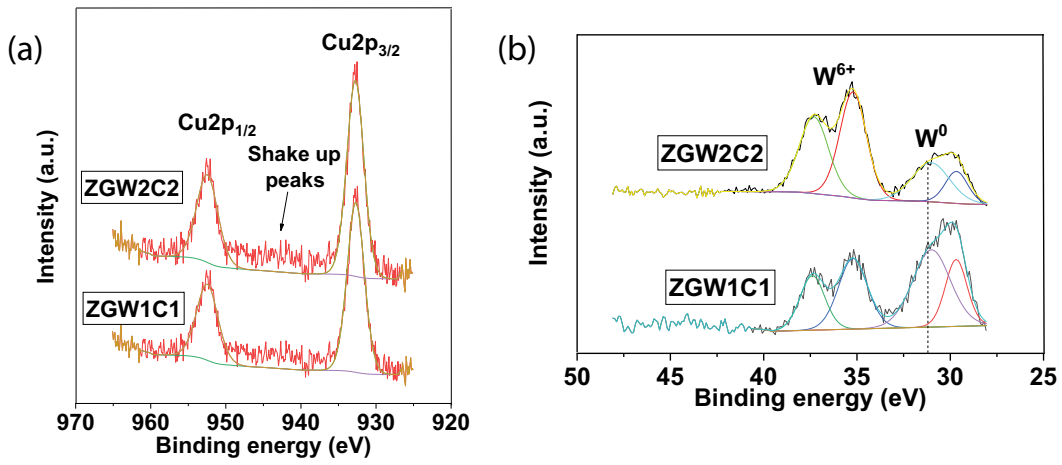

Fig. 8. The XPS spectra of (a) Cu2p, (b) W4f of ZGW1C1 and ZGW2C2 nanoparticle samples.

was increased up to 300 min, then it became almost stable, concluding that 300 min was the optimum reaction time Fig. 10. The decolorization percentage of MG dye was 3.8%, 7.7% and 71% for ZG, ZGW1C1 and ZGW2C2, respectively, within 300 min irradiation time at initial MG concentration of 40 mg/L, pH 5 (unadjusted pH of the solution) and 0.75 g/L catalyst dose. The major effect for the photocatalytic activity for Cu and W co-doped ZG was attributed to the band gap reduction shifting to the visible light region compared with over the parent one (Table 2).

Based on these results, a mechanism for photocatalytic degradation of MG dye was evident by the utilization of the visible light energy by $Ga_{2-x}Cu_xZr_{2-x}W_xO_7$ to excite its electrons from valence band to the conduction band. These electrons are trapped by oxygen molecule (dissolved oxygen), producing superoxide anion radical $O_2^{-\bullet}$ and also the HO^- groups on the surface receive a hole forming HO^- radicals. Both of $O_2^{-\bullet}$ and HO^- can assist MG degradation (Eqs. 2–7) [53]. Therefore, introducing W and Cu ions into ZG lattice significantly improves ZG photocatalytic activity.

$$Ga_{2-x}Cu_xZr_{2-x}W_xO_7 + h\upsilon(\lambda > 400\ nm) \rightarrow Ga_{2-x}Cu_xZr_{2-x}W_xO_7(e_{cb-} + h_{vb}) \quad (2)$$

$$Ga_{2-x}Cu_xZr_{2-x}W_xO_7(e_{cb-}) + O_2 \rightarrow Ga_{2-x}Cu_xZr_{2-x}W_xO_7 + O_2^{-\bullet} \quad (3)$$

$$h^+ + H_2O \rightarrow HO^\bullet \quad (4)$$

$$e^- + O_2 \rightarrow O_2^{-\bullet} \quad (5)$$

$$h_{vb} + MG \rightarrow \text{degradation by} - \text{product} \quad (6)$$

$$O_2^{-\bullet} + MG \rightarrow \text{degradation by} - \text{product} \quad (7)$$

4.2.2. The impact of catalyst loading

A series of experiments were performed by increasing the catalyst dosage from 0.5 to 1.25 g/L, with a dye concentration of 40 mg/L and the results are exhibited in Fig. 11. By increasing the catalyst dosage from 0.5 g to 0.75 g/L, the degradation performances significantly improved. As a result of the increase in catalysts dosage, the reactive sites increase which can correspondingly produce more reactive oxidative species. However, the increased amount of catalyst dispersed in the system (catalyst dosage above 0.75 g/L) will possibly increase light scattering and decrease the light penetration, resulting in diminution of degradation of MG. ZGW2C2 is considered as the superior in decolorization of the MG dye which attained 71% followed by 6.8% and 3.8% for ZGW1C1 and ZG, respectively at pH 5 and 40 mg/L MG concentration under visible light irradiation, at optimum catalyst dose 0.75 g/L within 300 min irradiation.

4.2.3. The impact of pH

The impact of pH on the photocatalytic degradation of MG was deliberated in the pH range 3–11. Fig. 12 revealed that photocatalytic degradation of MG augmented as the pH

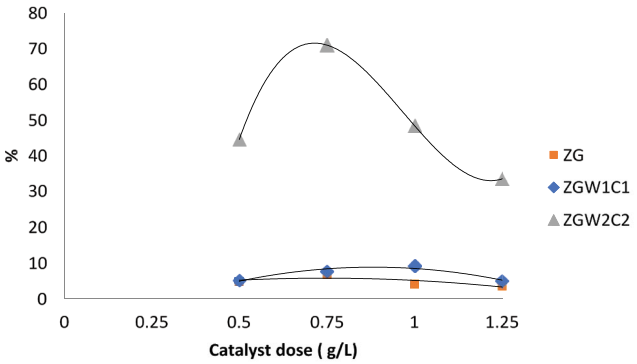

Fig. 11. The effect of catalyst dosage on MG degradation at pH 5 and 40 mg/L MG concentration under visible light irradiation.

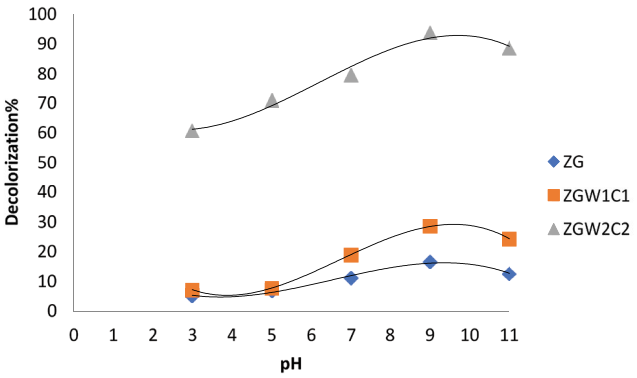

Fig. 12. The impact of pH on photocatalytic degradation of MG at 0.75 g/L catalyst dose and 40 mg/L MG concentration under visible light irradiation.

of the solution increased attaining the highest removal at pH 9 which was elected as the optimum pH value. By augmenting the pH > 9, the declination rate was diminished. For ZGW2C2 recorded the maximum decolorization percent (93.8%) at pH 9 within 300 min then a decrease to 88.7% at pH 10, which could be explained by the fact that at pH > 9, cationic form of MG is transformed into its neutral species, which is not caught towards the oxide surface due to the engagement of OH^- ions to the surface of the catalyst [54]. Accordingly, pH 9 is the optimum value.

4.2.4. The impact of malachite green concentration

Several concentrations of the MG dye (10, 20, 30, and 40 mg/L) were studied at 0.75 g/L ZGW2C2 dose and pH 9 under the visible light irradiation to deduce the impact of MG concentration on photocatalytic declination Fig. 13. The rate of photocatalytic degradation of dye diminished in order 0.02, .016, 0.013 and 0.001/min by increasing MG concentration. As a result of increasing MG concentration, the dye acts as an internal barrier and it does not allow the desired light intensity to arrive at the catalyst surface [54,55].

4.2.4. Degradation by-products of MG by GC-MS

UV-vis studies of the MG degradation by ZGW2C2 demonstrated that MG has a maximum absorbance peak

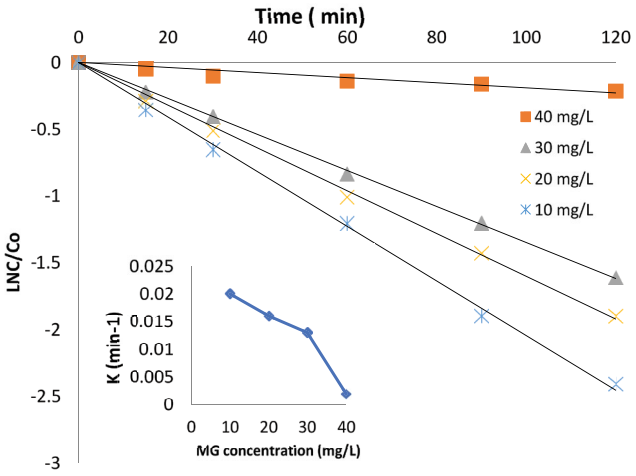

Fig. 13. Pseudo-first-order kinetics for different CV doses for ZGW2C2. Insert: The effect of different MG doses on the rate of the degradation reaction for ZGW2C2.

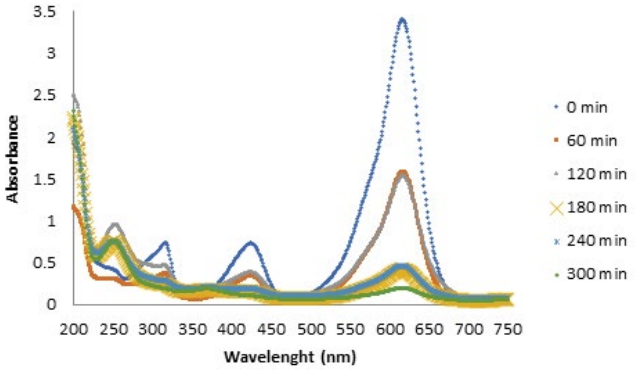

Fig. 14. The UV-vis studies of the MG degradation by ZGW2C2 under optimum operating condition.

at 617 nm Fig. 14. The main peak intensity decreased with boosting degradation time, while new adsorption peaks formed, which could be attributed to the cleavage of the chromophoric groups in the MG molecule firstly, that is, decolorization reactions took place, followed by mineralization reactions for the resulted intermediates [56].

The Gas chromatography- mass spectra identified the by-products of MG decolorization, based on the comparison of their relative retention time and mass spectra with those of NIST, WILEY library data of the GC-MS system Fig. 15.

From the experimental results of UV-VIS and GC-MS studies Fig. 16 we concluded that the main photocatalytic degradation and mineralization pathways of MG were the demethylation reactions on the amino group followed by the attack of hydroxyl radicals on the central carbon atoms. This was confirmed by the formation of new intermediates with m/z = 315 and 301 of N,N-dimethyl-4-((Z)-((Z)-4-(methylimino) cyclohexa-2,5-dien-1-ylidene) (phenyl) methyl) aniline and 4-((4-iminocyclohexa-2,5-dien-1-ylidene) (phenyl) methyl)-N,N dimethylaniline respectively in the MS spectra. Subsequently, the attack of hydroxyl radicals on the central carbon atoms forming the benzoic acid. Followed by the breaking of the aromatic cyclic group in the molecular structure which gives rise to the formation of some fatty acidic compounds of low molecular weight which may be degraded to carbon dioxide (m/z = 44) and water. Phenol measurement at the end of the experiment was found to be 0 mg/L to confirm the absence of phenol as by-product [57].

4.2.5. Reusability of the catalyst

In order to examine reusability, ten cycles for MG decolorization over the ZGW2C2 sample were carried out under the pre-optimized operating conditions. At the end of the reaction, the catalyst was recovered and washed with distilled water. The recovered catalyst was re-introduced for the new cycle, and so on. The removal efficiency of the dye MG was 93.8% in the first run, 91% in second run

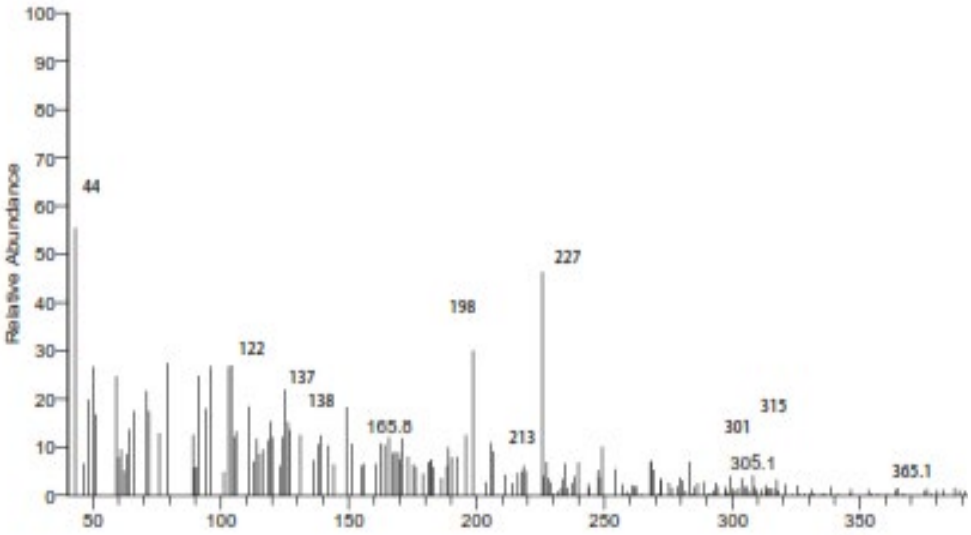

Fig. 15. The GC-MS mass spectra of photocatalytic degradation for MG using ZGW2C2 under optimum operating condition.

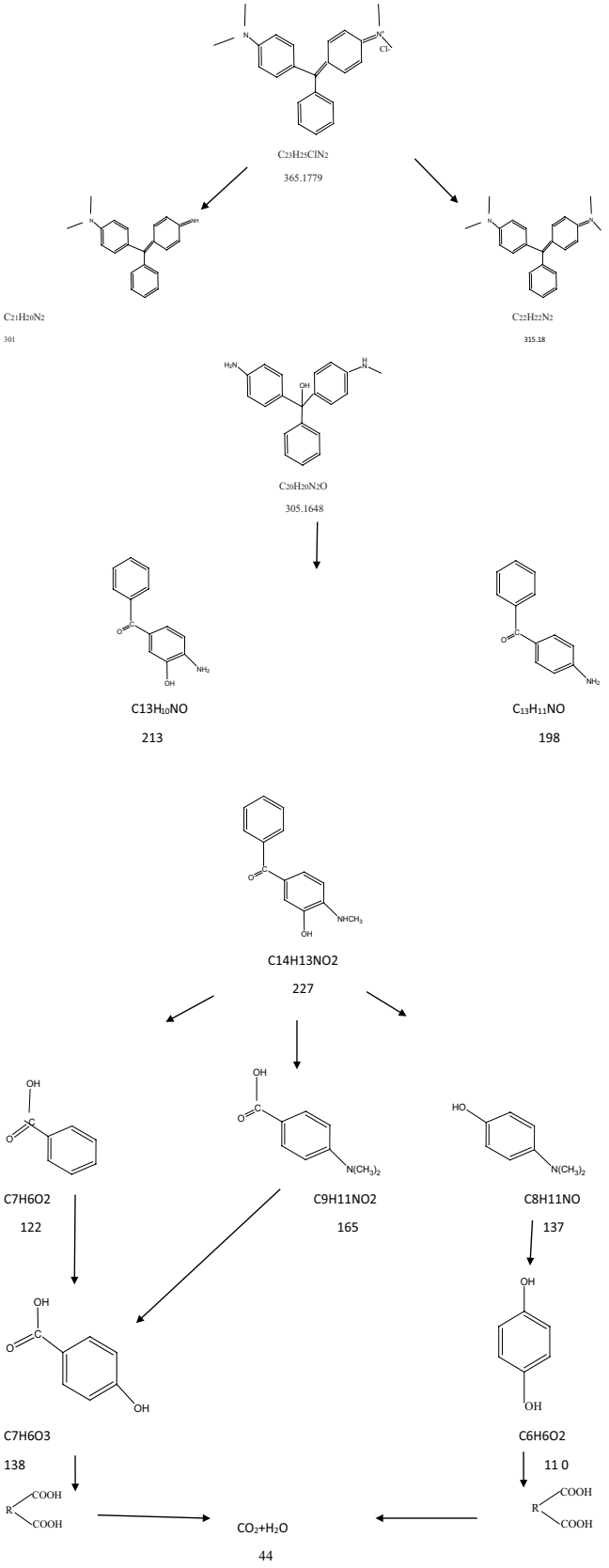

Fig. 16. Proposed pathway for photocatalytic degradation for MG.

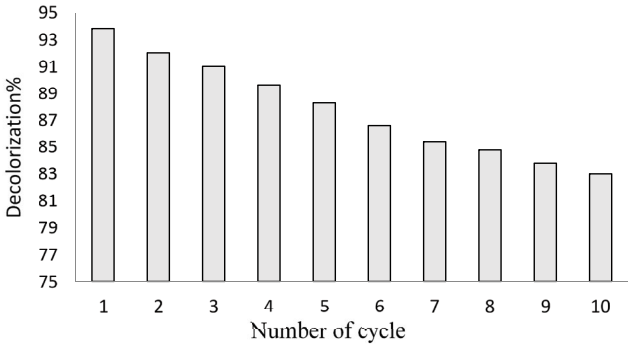

Fig. 17. The number of cycles for MG over ZGW2C2 sample under visible light at optimum conditions.

and remained higher than 83% in the tenth run, as shown in Fig. 17. The slight decrease can be attributed to the loss of photocatalysts between runs and some refractory intermediates adsorbed on their surface which is difficult to be destroyed which decreases the removal efficiency [54,58].

5. Conclusion

Nano-sized $Ga_{2-x}Cu_xZr_{2-x}W_xO_7$ samples with average crystallite size (4–7 nm) were prepared using Pechini method ($x = 0, 0.05, 0.15$). The characterization of the samples indicated that the samples are in the cubic fluorite phase structure, the band gap decreased from 4.95 eV for $Ga_2Zr_2O_7$ to 2.89 eV for $Ga_{1.85}Cu_{0.15}Zr_{1.85}W_{0.15}O_7$ sample. The photocatalytic decolorization results demonstrated that $Ga_{1.85}Cu_{0.15}Zr_{1.85}W_{0.15}O_7$ sample could be a promising photocatalyst for decolorizing of MG dyes under visible light irradiation. 93.8% of 40 ppm MG was removed in 300 min at pH 9. The reusability of the catalyst proved that the removal efficiency of the dye MG was 93.8% in the first run, 91% in the second run, and more than 83% in the tenth run. GC-MS study for degradation by-products was also conducted to estimate the proposed pathway for photocatalytic degradation for MG. In addition, the kinetic study indicated that MG dye photocatalytic degradation followed the Pseudo-first-order kinetics. Consequently, this work introduced a novel nano-sized $Ga_{1.85}Cu_{0.15}Zr_{1.85}W_{0.15}O_7$ photocatalyst for the degradation of dyes under visible light.

Acknowledgements

Authors would like to acknowledge the Science & Technology Development Fund in Egypt and the Scientific Research Support Fund in Jordan for financing that works through collaborative project number 21,734 in Egypt and number Egy-Jor/1/01/2015 in Jordan.

References

[1] C.I. Pearce, J.R. Lloyd, J.T. Guthrie, The removal of color from textile wastewater using whole bacterial cells: a review, Dyes Pigm., 58 (2003) 179–196.
[2] A.B. Dos Santos, F.J. Cervantes, J.B. van Lier, A review paper on current technologies for decolourization of textile wastewaters: perspectives for anaerobic biotechnology, Bioresour. Technol., 98 (2007) 2369–2385.

[3] A.G.S. Prado, J.D. Torres, E.A. Faria, S.C.L. Dias, Comparative adsorption studies of indigo carmine dye on chitin and chitosan, J. Colloid Interface Sci., 277 (2004) 43–47.
[4] M.M. Joshi, N.K. Labhsetwar, P.A. Mangrulkar, S.N. Tijare, S.P. Kamble, S.S. Rayalu, Visible light-induced photoreduction of methyl orange by N-doped mesoporous titania, Appl. Catal., A, 357 (2009) 26–33.
[5] S. Srivastava, R. Sinha, D. Roy, Toxicological effects of malachite green, Aquat. Toxicol., 66 (2004) 319–329.
[6] W. Cheng, S.-G. Wang, L. Lu, W.-X. Gong, X.-W. Liu, B.-Y. Gao, H.-Y. Zhang, Removal of malachite green (MG) from aqueous solutions by native and heat-treated anaerobic granular sludge, Biochem. Eng. J., 39 (2008) 538–546.
[7] Z. Bekçi, C. Özveri, Y. Seki, K. Yurdakoç, Sorption of malachite green on chitosan bead, J. Hazard. Mater., 154 (2008) 254–261.
[8] L.A. Pérez-Estrada, A. Agüera, M.D. Hernando, S. Malato, A.R. Fernández-Alba, Photodegradation of malachite green under natural sunlight irradiation: kinetic and toxicity of the transformation products, Chemosphere, 70 (2008) 2068–2075.
[9] M. Farhadian, M. Kazemzad, Photocatalytic degradation of malachite green by magnetic photocatalyst, Synth. React. Inorg. Met.-Org. Nano-Metal Chem., 46 (2016) 458–463.
[10] S.K. Kansal, M. Singh, D. Sud, Studies on photodegradation of two commercial dyes in aqueous phase using different photocatalysts, J. Hazard. Mater., 141 (2007) 581–590.
[11] C. Hachem, F. Bocquillon, O. Zahraa, M. Bouchy, Decolourization of textile industry wastewater by the photocatalytic degradation process, Dyes Pigm., 49 (2001) 117–125.
[12] M. Barjasteh-Moghaddam, A. Habibi-Yangjeh, Effect of operational parameters on photodegradation of methylene blue on ZnS nanoparticles prepared in presence of an ionic liquid as a highly efficient photocatalyst, J. Iran. Chem. Soc., 8 (2011) S169–S175.
[13] F. Sayılkan, M. Asiltürk, P. Tatar, N. Kiraz, E. Arpac, H. Sayılkan, Photocatalytic performance of Sn-doped TiO_2 nanostructured mono and double-layer thin films for Malachite Green dye degradation under UV and vis-lights, J. Hazard. Mater., 144 (2007) 140–146.
[14] N. Modirshahla, M.A. Behnajady, Photooxidative degradation of Malachite Green (MG) by UV/H_2O_2: Influence of operational parameters and kinetic modeling, Dyes Pigm., 70 (2006) 54–59.
[15] L. Papinutti, N. Mouso, F. Forchiassin, Removal and degradation of the fungicide dye malachite green from aqueous solution using the system wheat bran–*Fomes sclerodermeus*, Enzyme Microb. Technol., 39 (2006) 848–853.
[16] S. Sambasivam, D.P. Joseph, D.R. Reddy, B.K. Reddy, C.K. Jayasankar, Synthesis and characterization of thiophenol passivated Fe-doped ZnS nanoparticles, Mater. Sci. Eng., B, 150 (2008) 125–129.
[17] N. Daneshvar, M. Ayazloo, A.R. Khataee, M. Pourhassan, Biological decolorization of dye solution containing Malachite Green by microalgae *Cosmarium* sp., Bioresour. Technol., 98 (2007) 1176–1182.
[18] M.A. Behnajady, N. Modirshahla, M. Shokri, B. Vahid, Effect of operational parameters on degradation of Malachite Green by ultrasonic irradiation, Ultrason. Sonochem., 15 (2008) 1009–1014.
[19] M.Y. Ghaly, G. Härtel, R. Mayer, R. Haseneder, Photochemical oxidation of p-chlorophenol by UV/H_2O_2 and photo-Fenton process. A comparative study, Waste Manage., 21 (2001) 41–47.
[20] C.A.K. Gouvea, F. Wypych, S.G. Moraes, N. Duran, N. Nagata, P. Peralta-Zamora, Semiconductor-assisted photocatalytic degradation of reactive dyes in aqueous solution, Chemosphere, 40 (2000) 433–440.
[21] W.S. Kuo, L.N. Wu, Fenton degradation of 4-chlorophenol contaminated water promoted by solar irradiation, Sol. Energy, 84 (2010) 59–65.
[22] J. Tolia, M. Chakraborty, Z. Murthy, Photocatalytic degradation of malachite green dye using doped and undoped ZnS nanoparticles, Polish J. Chem. Technol., 14 (2012) 16–21.
[23] K.L. Ameta, N. Papnai, R. Ameta, Photocatalytic degradation of malachite green using nano-sized cerium-iron oxide, Orbital Electron. J. Chem., 6 (2014) 14–19.
[24] R. Ramachandran, M. Sathiya, K. Ramesha, A.S. Prakash, G. Madras, A.K. Shukla, Photocatalytic properties of $KBiO_3$ and $LiBiO_3$ with tunnel structures, J. Chem. Sci., 123 (2011) 517–524.
[25] A.R. Nanakkal, L.K. Alexander, Photocatalytic activity of graphene/ZnO nanocomposite fabricated by two-step electrochemical route, J. Chem. Sci., 129 (2017) 95–102.
[26] A. Khan, U. Alam, S. Zafar, M. Muneer, Fe (III)-grafted K-doped gC_3N_4/rGO composite photocatalyst with efficient activity towards the degradation of organic pollutants, J. Chem. Sci., 130 (2018) 142.
[27] J. Yan, Z. Chen, H. Ji, Z. Liu, X. Wang, Y. Xu, X. She, L. Huang, L. Xu, H. Xu, Construction of a 2D Graphene-Like MoS_2/C_3N_4 heterojunction with enhanced visible-light photocatalytic activity and photoelectrochemical activity, Chem. Eur. J., 22 (2016) 4764–4773.
[28] M. Malathi, K. Sreenu, G. Ravi, P.V. Kumar, C.H.S. Reddy, R. Guje, R. Velchuri, M. Vithal, Low-temperature synthesis of fluorite-type Ce-based oxides of composition $Ln_2Ce_2O_7$ (Ln = Pr, Nd and Eu): photodegradation and luminescence studies, J. Chem. Sci., 129 (2017) 1193–1203.
[29] M.C. Hatnean, M.R. Lees, G. Balakrishnan, Growth of single-crystals of rare-earth zirconate pyrochlores, $Ln_2Zr_2O_7$ (with Ln = La, Nd, Sm, and Gd) by the floating zone technique, J. Cryst. Growth, 418 (2015) 1–6.
[30] B.P. Mandal, A.K. Tyagi, Pyrochlores: potential multifunctional materials, Barc Newsl., 313 (2010) 6–13.
[31] M.P. Pechini, Method of Preparing Lead and Alkaline Earth Titanates and Niobates and Coating Method Using The Same to Form a Capacitor, US3330697A, 1967.
[32] A.J. Carrillo, D.P. Serrano, P. Pizarro, J.M. Coronado, Design of Efficient Mn-Based Redox Materials for Thermochemical Heat Storage at High Temperatures, AIP Conf. Proc., 2016, p. 50009.
[33] P.C. Ribeiro, A.C.F. de M. Costa, R.H.G.A. Kiminami, J.M. Sasaki, H.L. Lira, Synthesis of TiO_2 by the pechini method and photocatalytic degradation of methyl red, Mater. Res., 16 (2013) 468–472.
[34] A.E. Danks, S.R. Hall, Z. Schnepp, The evolution of 'sol–gel' chemistry as a technique for materials synthesis, Mater. Horiz., 3 (2016) 91–112.
[35] T.O.L. Sunde, T. Grande, M.-A. Einarsrud, Modified Pechini Synthesis of Oxide Powders and Thin Films, Handbook of Sol-Gel Science and Technology, T.O.L. Sunde, T. Gd. M.-A. Einarsrud, Modif. Pechini Synth. Oxide Powders Thin Film. Handb. Sol-Gel Sci. Technol., 1–30.Y., 2016, pp. 1–30.
[36] L. Zhang, J. Yang, J. Li, A novel composite cathode for intermediate temperature solid oxide fuel cell, J. Power Sources, 269 (2014) 723–726.
[37] APHA, Standard Method for Examination of Water and Wastewater, 23rd ed., American Public Health Association, 2017.
[38] T.J.B. Holland, S.A.T. Redfern, Unit cell refinement from powder diffraction data: the use of regression diagnostics, Mineral. Mag., 61 (2006) 65–77.
[39] R.D. Shannon, Revised effective ionic radii and systematic studies of interatomic distances in halides and chalcogenides, Acta Crystallogr., Sect. A: Found. Crystallogr., A32 (1976) 751–767.
[40] T.S. Jamil, E.S. Mansor, R.A. Nasr, Degradation of Lindane using two nanosized BiOXs and their heterojunction under visible light, 57 (2016) 14750–14761.
[41] Y. Zhang, J. Yan, Q. Li, C. Qu, L. Zhang, W. Xie, Optical and structural properties of Cu-doped β-Ga_2O_3 films, Mater. Sci. Eng., B, 176 (2011) 846–849.
[42] K. Sayama, H. Arakawa, Effect of Na_2CO_3 addition on photocatalytic decomposition of liquid water over various semiconductor catalysis, J. Photochem. Photobiol., A, 77 (1994) 243–247.
[43] K. Sayama, H. Arakawa, Effect of carbonate addition on the photocatalytic decomposition of liquid water over a ZrO_2 catalyst, J. Photochem. Photobiol., A, 94 (1996) 67–76.
[44] M. Uno, A. Kosuga, M. Okui, K. Horisaka, H. Muta, K. Kurosaki, S. Yamanaka, Photoelectrochemical study of lanthanide

zirconium oxides, $Ln_2Zr_2O_7$ (Ln = La, Ce, Nd, and Sm), J. Alloys Compd., 420 (2006) 291–297.
[45] H.A. Abbas, T.S. Jamil, F.F. Hammad, Synthesis, characterization and photocatalytic activity of nano sized undoped and Ga doped $SrTi_{0.7}Fe_{0.3}O_3$ for 2,4,6-trichlorophenol photodegradation, J. Environ. Chem. Eng., 4 (2016) 2384–2393.
[46] H.A. Abbas, T.S. Jamil, F.F. Hammad, Journal of environmental chemical engineering synthesis, characterization and photocatalytic activity of nano-sized photodegradation, Biochem. Pharmacol., 4 (2016) 2384–2393.
[47] T.S. Jamil, H.A. Abbas, R.A. Nasr, A.A. El-Kady, M.I.M. Ibrahim, Detoxification of aflatoxin B1using nano-sized Sc-doped $SrTi_{0.7}Fe_{0.3}O_3$ under visible light, J. Photochem. Photobiol., A, 341 (2017) 127–135.
[48] H.A. Abbas, A.M. Youssef, F.F. Hammad, A.M.A. Hassan, Z.M. Hanafi, Electrical properties of nano-sized indium tin oxide (ITO) doped with CuO, Cr_2O_3 and ZrO_2, J. Nanopart. Res., 16 (2014) 2518.
[49] M.C. Biesinger, L.W.M. Lau, A.R. Gerson, R.S.C. Smart, Resolving surface chemical states in XPS analysis of first row transition metals, oxides and hydroxides: Sc, Ti, V, Cu and Zn, Appl. Surf. Sci., 257 (2010) 887–898.
[50] Z. Liang, L. Zhao, W. Meng, C. Zhong, S. Wei, B. Dong, Z. Xu, L. Wan, S. Wang, Tungsten-doped vanadium dioxide thin films as smart windows with self-cleaning and energy-saving functions, J. Alloys Compd., 694 (2017) 124–131.
[51] B. Yous, S. Robin, A. Donnadieu, G. Dufour, C. Maillot, H. Roulet, C. Senemaud, Chemical vapor deposition of tungsten oxides: a comparative study by X-ray photoelectron spectroscopy, X-ray diffraction and reflection high energy electron diffraction, Mater. Res. Bull., 19 (1984) 1349–1354.
[52] S.E.A.S. El-deen, N.S. Ammar, T.S. Jamil, Adsorption behavior of Co (II) and Ni (II) from an aqueous solutions onto titanate nanotubes, 24 (2016) 455–466.
[53] M.A. Rauf, M.A. Meetani, S. Hisaindee, An overview on the photocatalytic degradation of azo dyes in the presence of TiO_2 doped with selective transition metals, Desalination, 276 (2011) 13–27.
[54] R. Rathore, R. Ameta, S.C. Ameta, Photocatalytic degradation of malachite green over nickel vanadate powder, 4 (2014) 213–220.
[55] T.S. Jamil, H.A. Abbas, R.A. Nasr, R.-N. Vannier, Visible light activity of $BaFe_{1-x}Cu_xO_{3-\delta}$ as photocatalyst for atrazine degradation, Ecotoxicol. Environ. Saf., 163 (2018) 620–628.
[56] S.K. Ray, D. Dhakal, S.W. Lee, Insight into malachite green degradation, Mechanism and pathways by morphology-tuned a -$NiMoO_4$ Photocatalyst, 4 (2018) 552–563.
[57] G.A.O. Guandao, Z. Aiyong, Z. Meng, C. Jinlong, Z. Quanxing, Photocatalytic degradation mechanism of malachite green under visible light irradiation over novel Biomimetic Photocatalyst HMS-FePcs, Chin. J. Catal., 29 (2008) 426–430.
[58] X. Meng, Z. Zhang, Synthesis, analysis, and testing of BiOBr-Bi_2WO_6 photocatalytic heterojunction semiconductors, Int. J. Photoenergy, 2015 (2015), https://doi.org/10.1155/2015/630476.

Supplementary information

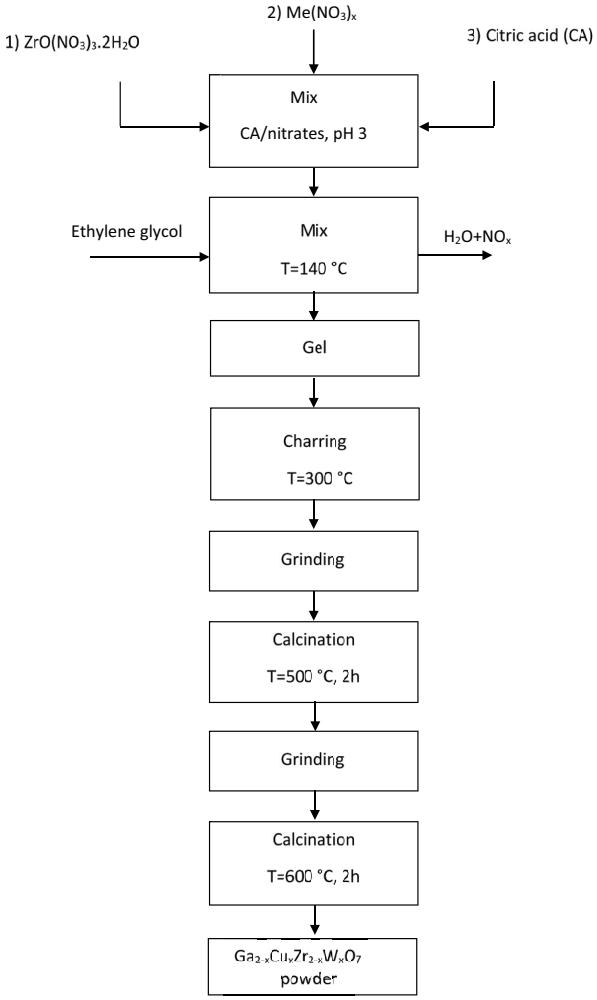

Fig. S1. Flow chart for the full process of polymeric precursor synthesis and preparation of $Ga_{2-x}Cu_xZr_{2-x}W_xO_7$ powder.

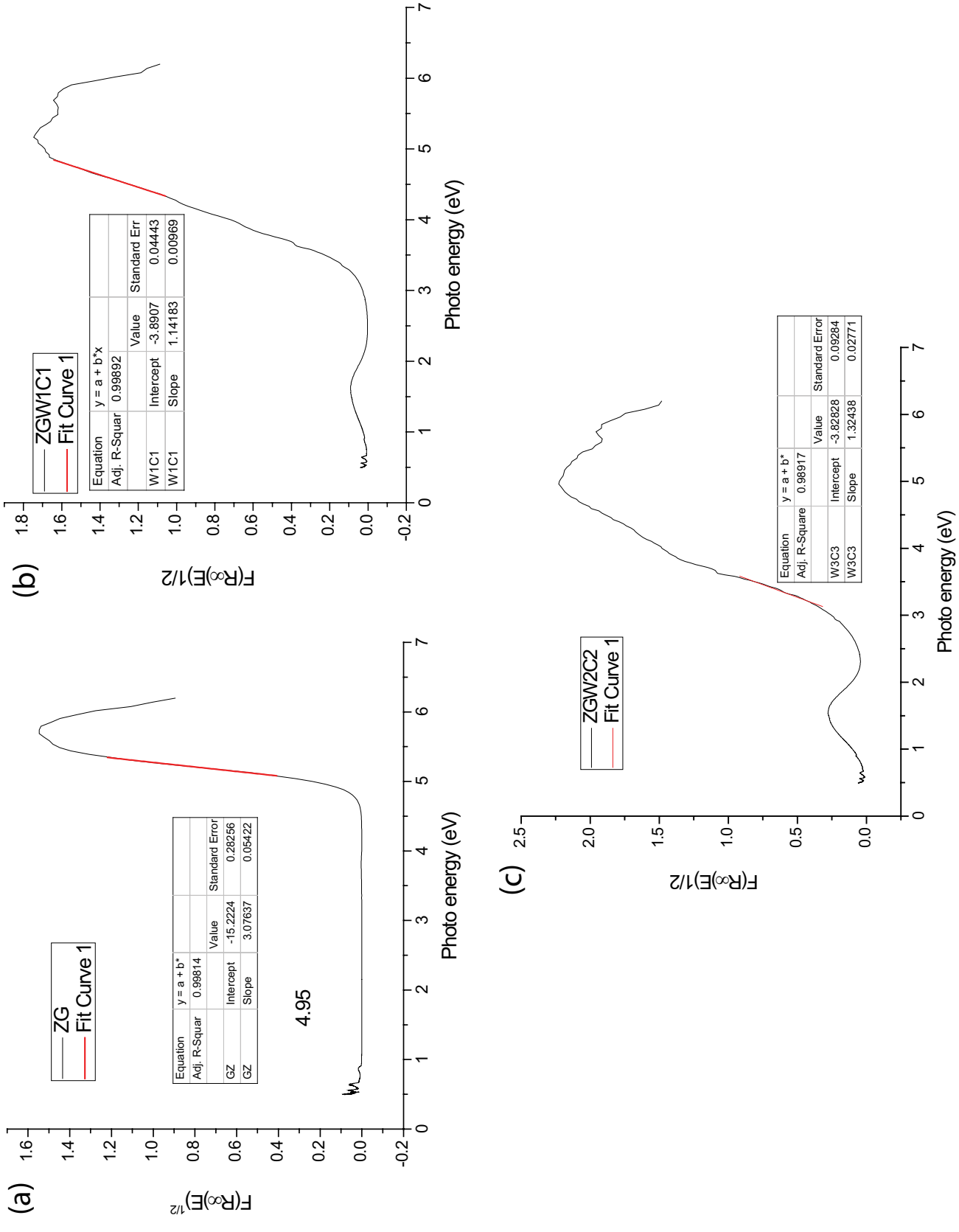

Fig. S2. Linear fit for the estimation of the band gap energy for ZG, ZGW1C1 and ZGW2C2 samples.

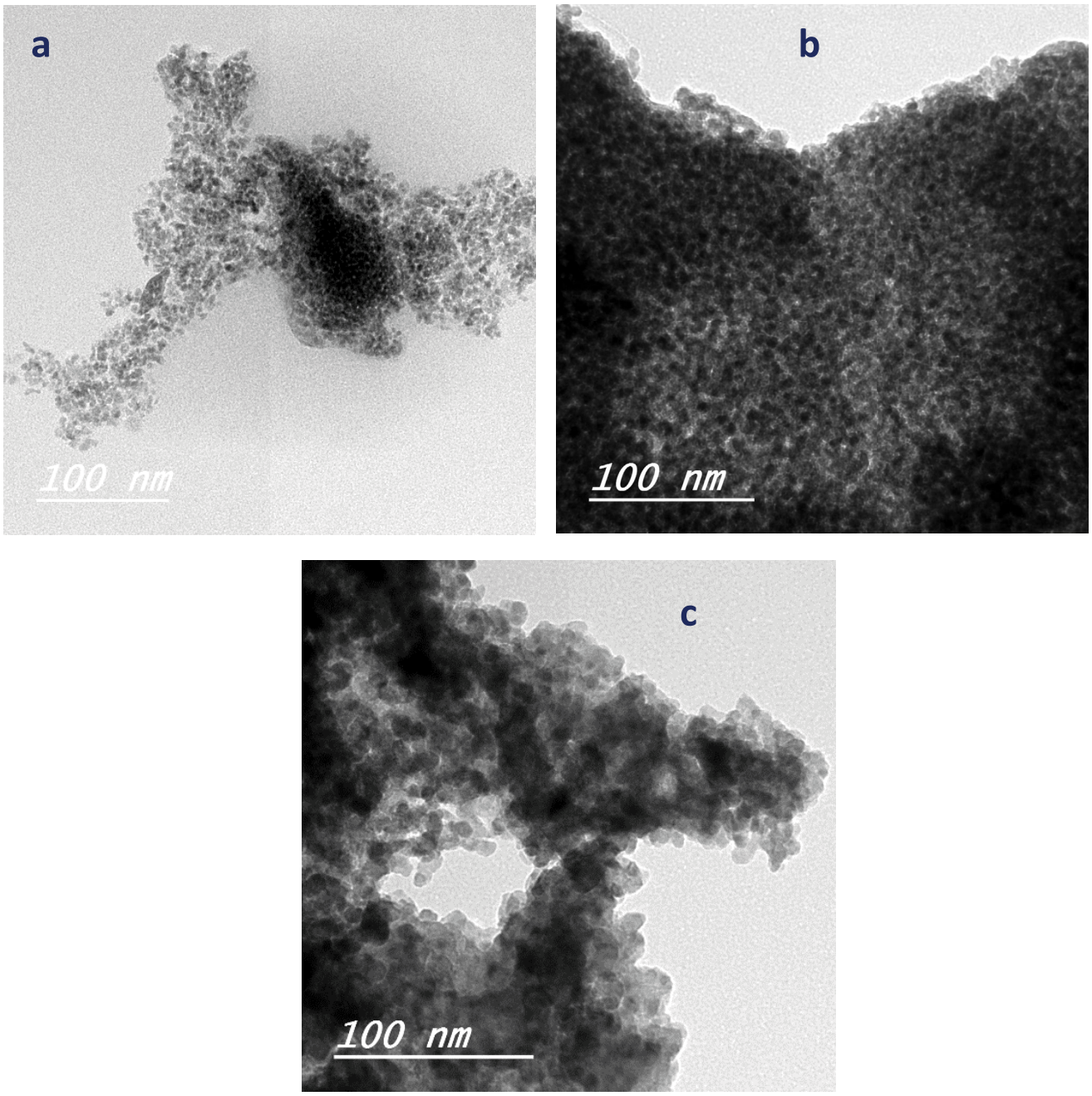

Fig. S3. TEM micrograph of (a) ZG, (b) ZGW1C1, and (c) ZGW2C2 samples calcined at 600°C/2h.

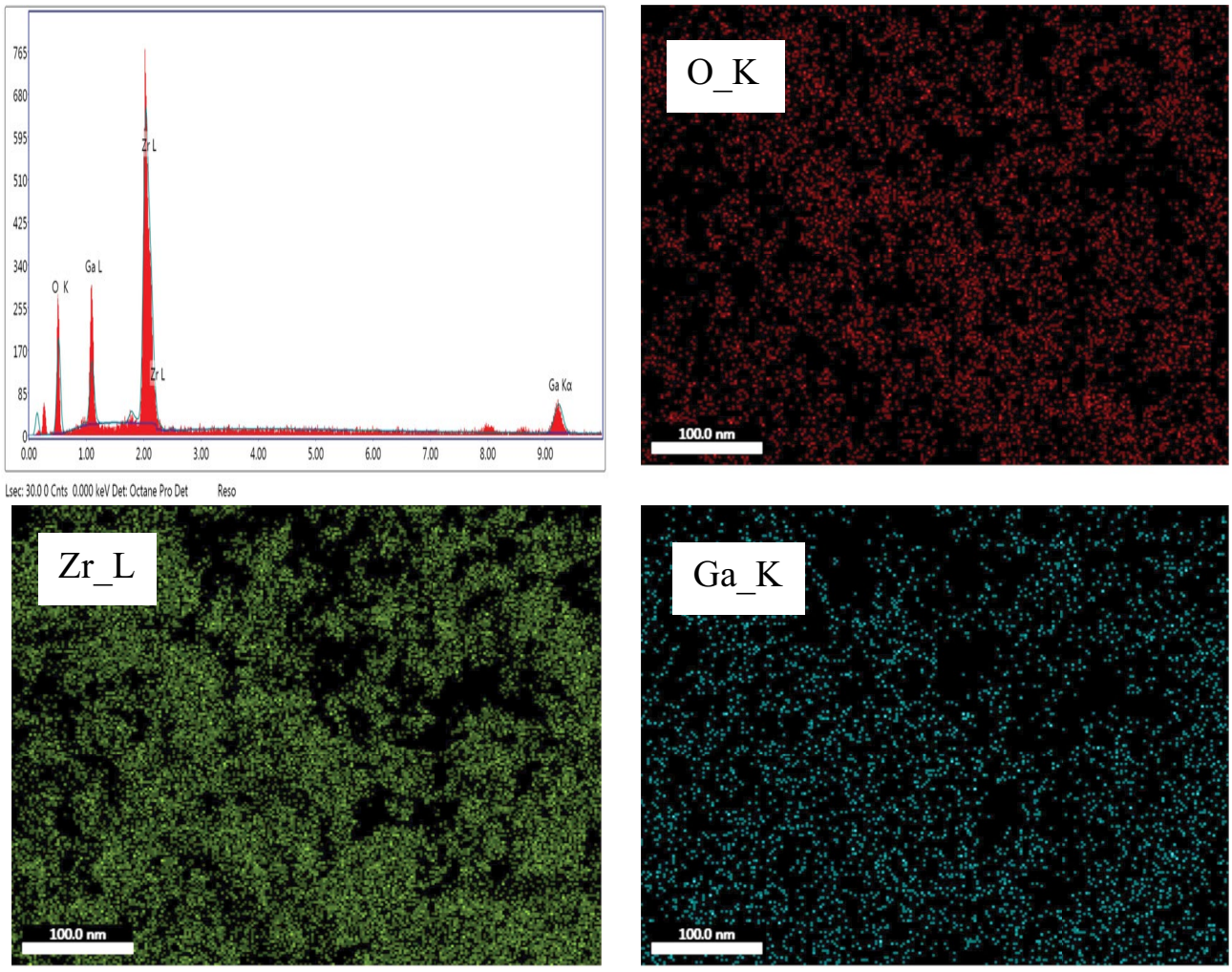

Fig. S4. The EDX and elemental mapping of the ZG sample.

Table S1
The elemental composition for ZG, ZGW1C1 and ZGW2C2 samples obtained from XPS analysis

Sample	Zr (at.%)	Ga (at.%)	W (at.%)	Cu (at.%)	O (at.%)
ZG	18.18	18.18	–	–	63.63
ZGW1C1	17.73	17.73	0.45	0.45	63.64
ZGW2C2	16.82	16.82	1.36	1.36	63.64

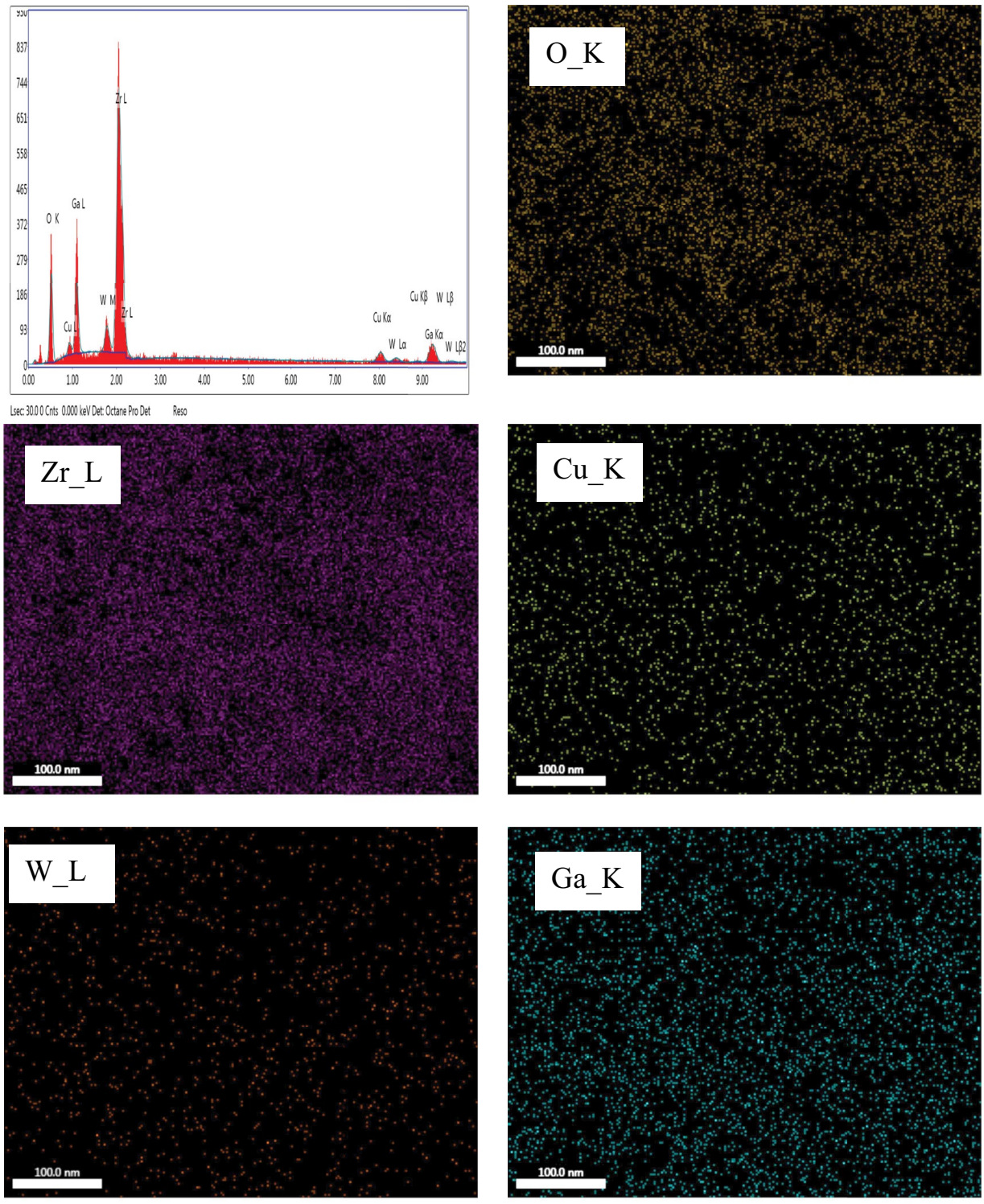

Fig. S5. The EDX and elemental mapping of the ZGW1C1 sample.